Long-range strains and the effects of applied field at 180° ferroelectric domain walls in lithium niobate

Terrence Jach,[1] Sungwon Kim,[2] Venkatraman Gopalan,[2] Stephen Durbin,[3] and David Bright[1]
[1]*Chemical Science and Technology Laboratory, National Institute of Standards and Technology, Gaithersburg, Maryland 20899-8371, USA*
[2]*Materials Research Institute and Department of Materials Science and Engineering, Pennsylvania State University, University Park, Pennsylvania 16802, USA*
[3]*Department of Physics, Purdue University, West Lafayette, Indiana 47907, USA*
(Received 12 May 2003; published 27 February 2004)

Ferroelectric domains with antiparallel polarization are readily induced in congruent $LiNbO_3$ with electric fields above 240 kV/cm at room temperature. Even in the absence of external fields, these 180° walls exhibit wide regions of shear strain, on the order of 10^{-5}, within a 10-μm range of the domain walls. Using x-ray topography on samples while applying electric fields of 0–90 kV/cm, we have observed large-scale reversible domain changes. A detailed strain analysis of the piezoelectric behavior at the domain walls, as well as within the domains, indicates that substantial surface displacement is associated with the high contrast of ferroelectric domains in x-ray topographs. These observations show that long-range strain interactions due to applied fields are present around domain walls long before permanent changes are induced.

DOI: 10.1103/PhysRevB.69.064113 PACS number(s): 77.80.Dj, 77.65.−j, 77.84.Dy, 61.10.−i

I. INTRODUCTION

The technology surrounding ferroelectric domains is diverse, covering nonvolatile memory as well as piezoelectric, pyroelectric, and nonlinear optical applications. In particular, the creation of antiparallel ferroelectric domains of various shapes and sizes in $LiNbO_3$ crystals is key to nonlinear optics[1] and electro-optics.[2] In realizing these applications, an understanding of the underlying physics of the local structure and the dynamics of ferroelectric domain walls is important.

In contrast to ferromagnetic domain walls, where the magnetic polarization can rotate continuously across a Bloch wall from one orientation to another, the strong coupling between ferroelectric polarization and lattice strain restricts the polarization in ferroelectrics to specific crystallographic directions. Landau-Ginzburg phenomenological models describe abrupt polarization profiles consisting of kinks or solitons.[3–5] Recent first principles calculations in the most important class of oxygen octahedra ferroelectrics show that the polarization change across a 180° ferroelectric domain wall should be atomically sharp. As a consequence, while the antiparallel (180°) ferromagnetic walls can easily be micrometers wide, ferroelectric walls are expected to have intrinsic widths of the order of 1–2 lattice constants.[6]

Furthermore, since the lattice polarization is coupled to the spontaneous lattice strain through electrostriction, the local spontaneous strain width arising from the polarization gradient across such domain walls is expected to be sharp as well.[5–8]

Experimentally, there are a range of results reported for the intrinsic wall widths of fixed domains: 2 nm for 90° domain walls in $PbTiO_3$ using electron microscopy,[9] 150 nm for 180° domains in $LiNbO_3$ using AFM,[10] and $\leqslant$300 nm for $LiNbO_3$ using x-ray topography.[11]

In this work, we provide strong evidence that the local strain of an antiparallel domain wall can be spatially extended, in contrast to the theoretical expectation of a sharply localized spontaneous strain region, in a ferroelectric with extrinsic defect contributions. We present detailed experimental and theoretical analysis of the x-ray topographic imaging of local domain wall strains in ferroelectric lithium niobate in the absence and presence of external electric fields.

The crystals we studied are not of the stoichiometric ($LiNbO_3$) composition, but rather of the congruent composition $(Li_{0.95}\square_{0.04}Nb_{0.01})NbO_3$, in which the lithium deficiency (and niobium excess) in the lattice exists as lithium vacancies ($\square_{Li}$) and niobium antisites (Nb_{Li}).[12] A previous study under zero external field found unexpectedly wide regions (0.3–1 μm) of optical birefringence adjacent to a ferroelectric domain wall in congruent $LiTaO_3$ (isostructural with $LiNbO_3$) using near-field scanning microscopy.[13] Strain images observed in x-ray topographs of both lithium niobate and tantalate appear to support this.[14] In this study, we quantitatively characterize the type and magnitude of the observed strains in detail using x-ray rocking curves and topographs. We then show that under an applied electric field that is substantially lower than the coercive field required for domain motion (~240 kV/cm), the domain wall strains extend over 100 μm or more, primarily arising through the piezoelectric effect. In the process, we observe x-ray focusing and defocusing effects due to surface distortions, which make ferroelectric domains behave as x-ray mirrors.

Generalized strains along different axes of $LiNbO_3$ have been previously observed by x-ray topography during the application of an electric field.[15,16] In this study, we compare experimentally measured strains in the vicinity of domains and domain walls and compare them with systems modeled by finite element analysis. These numerical simulations show clear qualitative agreement, while revealing significant quantitative differences. We consider physical reasons that could account for this.

II. EXPERIMENT

The experiment consisted of x-ray topography carried out by Bragg diffraction from single crystals of $LiNbO_3$. Topographs were obtained with and without the application of electric fields by high resolution real-time imaging. The work was carried out on the 1-ID and 4-ID beamlines of the SRI-CAT at the Advanced Photon Source, at Argonne National Laboratory. Each beamline was equipped with a symmetric Si(111) double crystal monochromator that we operated at 8.532 keV.

The beamlines produce an x-ray beam with a vertical divergence of less than 36 μrad. More importantly, the local divergence angle on a microscopic area of the crystal due to the source size and distance from the undulator is 1.4 μrad. This is far smaller than the width of the symmetric double crystal Si(111) monochromator Bragg reflection (44.5 μrad) or the intrinsic rocking curve width of $LiNbO_3$ (16.3 μrad). It is thus possible to do excellent topography using the symmetric crystal monochromator.

The samples studied here were *z*-cut congruent $LiNbO_3$ single crystals (uniaxial direction normal to the substrate). The crystal dimensions were approximately 3×3 cm^2. Starting from a single domain state at room temperature, domains of reverse polarity were created by applying electric fields of 240 kV/cm at room temperature, as described in detail elsewhere.[17] The nucleation and growth of domains was uncontrolled, and the final domain configuration was multiple hexagonal domains within a constant matrix domain state separated by 180° domain walls. For diffraction with an applied electric field, conductive electrodes consisting of a 100-nm film of amorphous carbon were deposited on either side over an approximately 1×1-cm^2 area in the center of the crystal. The crystals were mounted on an insulated stage in a six-circle goniometer.

Regions of the order of 1–2 mm^2 illuminated by the incident beam were imaged in the (00.12) Bragg reflection using a magnifying x-ray camera. The camera consisted of a Gd oxysulfide sputtered fluorescent thin film deposited on a magnifying optical taper which is coupled to a cooled CCD detector with a 12-bit readout accuracy. The fluorescent film was relatively insensitive to third harmonic radiation from the monochromator. The lateral resolution of the combination was 6 μm over a 3×3-mm^2 field. The camera was mounted 0.47 m from the sample crystal. The images were recorded with integration times of 50 ms–1 s, depending on the degree of attenuation employed downstream in the diffracted beam.

The run began with a Bragg rocking curve of the selected region of the crystal measured with a NaI scintillation detector. X-ray topographic images were then recorded as the electric field was raised to successively higher values, reduced to zero, and then raised to the same values with the opposite polarity. This was done to observe the maximum range possible when the breakdown limit for the specimen with electrodes was unknown ahead of time. It was readily observed that the reaction of the specimen to the field did not show hysteresis over the range that we were able to apply and was completely reproducible. The specimen sometimes displayed abrupt changes in strain as the field was increased, but the strain state was consistently the same for the same applied field. Topographs were obtained in real time with applied electric fields of up to ±90 kV/cm without breakdown.

III. DOMAINS IN ZERO APPLIED FIELD

A *z*-cut crystal with a thickness of 0.3 mm was used to study reflection from stable domains with zero applied field. A series of (00.12) Bragg reflection images is shown in Fig. 1 for three slightly different angles of incidence. The ferroelectric polarization direction, P_s in a domain is in the $+z$ direction (outward normal to image plane in Fig. 1) and in the $-z$ direction in the matrix outside the hexagonal domains.

There are three mechanisms which contribute to the visibility of ferroelectric domains in congruent $LiNbO_3$: (a) the difference in the structure factor between the antiparallel domain and the surrounding completely polarized single crystal matrix, (b) any difference in lattice spacing in the volume of diffraction, and (c) distortions of the bulk resulting in displacement of the surface normal from the ordinary crystallographic axis.

The presence of lithium vacancies and niobium antisite defects in the congruent material give rise to a remnant internal field such that the antiparallel domain is not simply a symmetry inversion of the polarized matrix.[18] We have calculated the contribution to the Bragg intensity due to the different structure factors between reversed domains in congruent $LiNbO_3$. For the (00.12) and $(00.\overline{12})$ reflections at 8.5 keV, the difference is 9%. The remaining contrast between domains and their surrounding matrix is evidently the result of surface distortions and changes in the lattice spacing.

Figure 1(b) corresponds to the reflection at the Bragg peak. The rocking curve of the reflection is shown as a function of the nominal value of the Bragg angle from the goniometer in Fig. 1(d) (the calculated Bragg angle at this energy was $\theta_B=39.0°$). Figures 1(a) and 1(c) show the topograph in the crystal region (area 1×2 mm^2) when the crystal is rocked about the diffraction peak. The measured full width at half maximum of the rocking curve, which included the distortion effect of domains, was $\Delta\theta_B=0.0063°=110$ μrad. The incidence plane in the image is vertical, being parallel to the crystallographic *y* axis. From Fig. 1(a) to Fig. 1(c), we rotated the sample through 0.006° in steps of $\Delta\theta=0.0005°$ towards increasing incidence angle.

The wall types 1, 2, 5, and 6 [labels in Fig. 1(b)] in each hexagonal domain are not parallel to the incidence plane, and show an enhanced contrast over a wide region (~10 μm wide) of associated strain in Figs. 1(a) and 1(c). The wall types 3 and 4, on the other hand, are parallel to the incidence plane and show the least contrast. This contrast phenomenon reveals itself more clearly on moving away from the Bragg peak, and suggests a curvature of lattice planes in the wall region in going from one domain to the other that can be described by the strain component dz/du, where $\hat{u}$ is the coordinate normal to a wall but parallel to the average plane

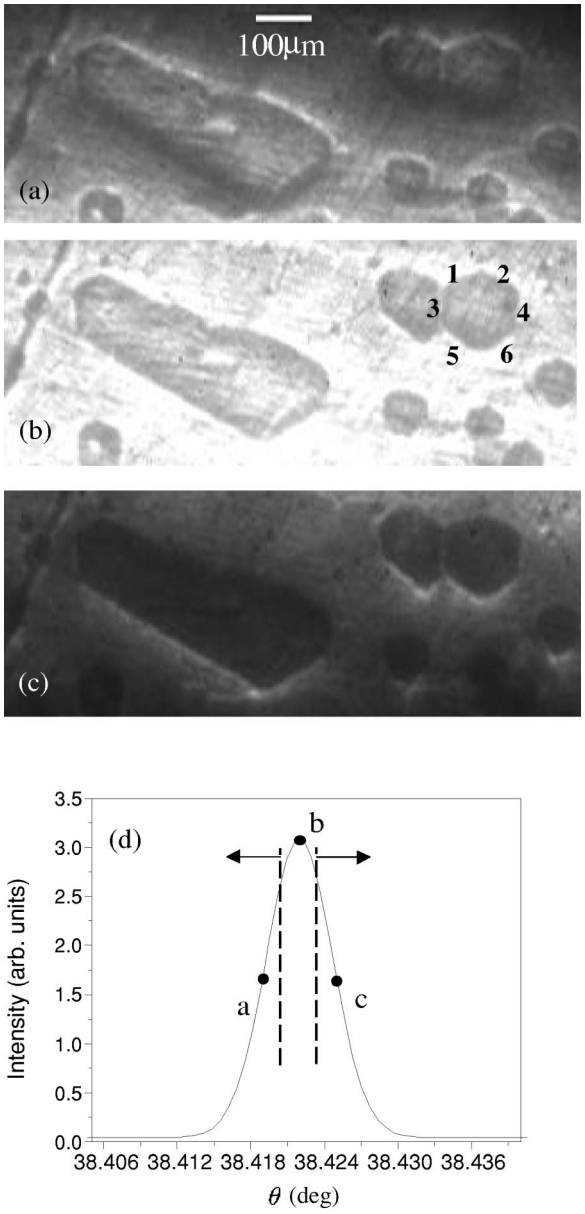

FIG. 1. (a) Bragg topograph of $LiNbO_3$ crystal at position *a* ($\theta_B - 0.003°$) on the (00.12) rocking curve. (b) Bragg topograph of $LiNbO_3$ crystal at position *b* (θ_B) on the (00.12) rocking curve. (c) Bragg topograph of $LiNbO_3$ crystal at position *c* ($\theta_B + 0.003°$) on the (00.12) rocking curve. (d) (00.12) Bragg rocking curve for the $LiNbO_3$ sample crystal, and the arbitrary intensity as a function of nominal goniometer Bragg angle (calculated $\theta_B = 39.0°$). The region to the left of the left dashed line corresponds to the observation of bright borders at walls 1 and 2; the region to the right of the right dashed line corresponds to bright borders at walls 5 and 6.

of the surface, and $\hat{z}$ is the coordinate along the direction of ferroelectric polarization (normal to the image plane in Fig. 1). Such a wall curvature would be expected to cause a deviation of the incidence angle, θ from θ_B and influence the Bragg diffraction condition most strongly when the wall is perpendicular to the incidence plane, and least when the wall is parallel to the incidence plane. This is consistent with the experimental observations in Fig. 1.

A closer inspection reveals that the contrast of the set of walls (1, 2) is opposite to the contrast of the set of walls (5, 6). That is, if one set of walls (1, 2), is bright, the other set (5, 6) is dark [seen in Fig. 1(a) and, conversely, Fig. 1(c)]. The projections of the incident and diffracted x-ray wave vectors onto the image plane of Fig. 1 point in the $-y$ direction with respect to the domain. In Fig. 1(a), the local region near domain walls (1, 2) would appear to be closer to the Bragg condition, thus making them bright, as compared to domain walls (5, 6), which are farther from the Bragg condition, giving them a darker contrast. This situation is reversed in Fig. 1(c). This provides additional evidence for the domain wall curvature, which we now proceed to estimate.

The maximum in the Bragg peak of an average region (predominantly strain-free regions away from the walls) corresponds to Fig. 1(b) where the surface curvature at all domain walls is equally off the ideal Bragg condition. However, the Bragg condition for the local region near walls (1, 2) corresponds approximately to Fig. 1(a) and that for walls (5, 6) corresponds approximately to Fig. 1(c). Knowing the difference between the Bragg angles between these frames, we therefore estimate that the $\Delta\theta_B(1,2) = \theta_B(1,2) - \theta_B(\text{center}) = -0.0030° \pm 0.0015°$ and similarly, $\Delta\theta_B(5,6) = +0.0030° \pm 0.0015°$. Converting these angles to radians, we therefore very roughly estimate the shear strain at these domain walls as $= dz/du \approx \Delta\theta_B/\cos\varphi$, where z is positive along the outward normal to the image plane in Fig. 1, $\hat{u}$ is the outward normal (pointing into the matrix domain) to the domain wall in the image plane, and φ is the angle between the domain wall and the incidence plane (here $\varphi \approx 30°$). In $LiNbO_3$, the domain walls are parallel to the crystallographic y axis ($[1\bar{1}00]$ direction). The sheer strain normal to the wall ε_{zu} is, by symmetry, equivalent to ε_{zx}. Therefore, $\varepsilon_{zx}(1 \text{ and } 2) \approx -6\times10^{-5} \pm 3\times10^{-5}$ and $\varepsilon_{zx}(5 \text{ and } 6) \approx +6\times10^{-5} \pm 3\times10^{-5}$.

Given that $\Delta x \sim 10\ \mu$m is the approximate strain width in the image plane observed in Fig. 1, the displacement observed is given by $\Delta z = \varepsilon_{zx}\Delta x \approx 0.6$ nm. This implies that when viewing the $+z$ face of the matrix domain, the region inside the hexagonal domains (with polarization along $-z$) is raised by $\sim$0.6 nm in height with respect to the oppositely polarized surrounding matrix region. This is also consistent with a similar surface step across a domain wall observed using near-field optical microscopy (NSOM) in the isostructural $LiTaO_3$ crystals.[13] X-ray imaging of the $-z$ face of the matrix domain was not performed. However, from NSOM studies, the other face (corresponding to the $-z$ of the matrix domain and $+z$ of the hexagonal domain) in the isostructural $LiTaO_3$ appears to show a depression of $\sim$0.6 nm inside the hexagonal domain area. In a cross section of the crystal, therefore, the inverted hexagonal domain region would appear to have shifted through the entire thickness giving rise to a 0.6-nm step projection on the $+z$ face of the matrix domain and a depression on the $-z$ face of the matrix domain.

We finally note that the large observed x-ray strains in congruent composition lithium niobate under no external

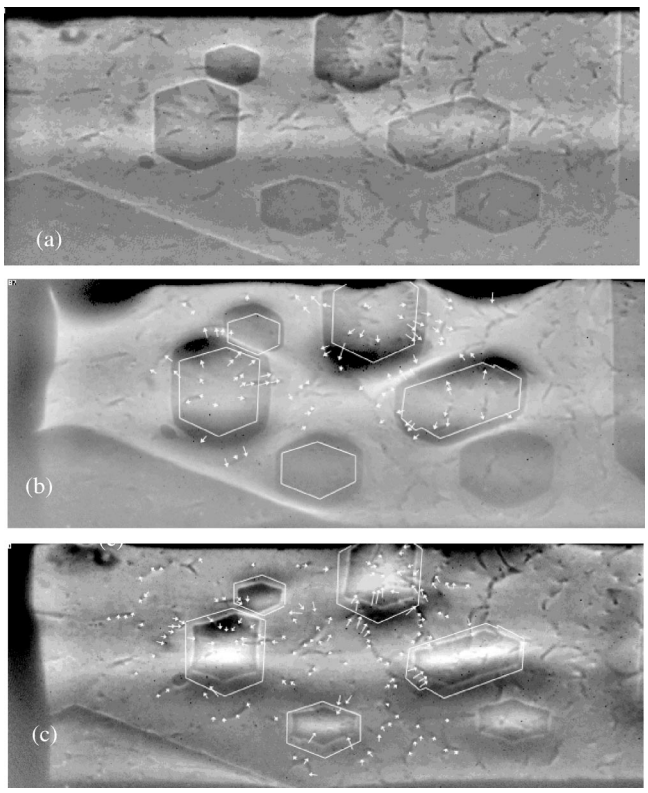

FIG. 2. (00.12) Bragg topograph of $LiNbO_3$ crystal (a) at applied voltage $V=0$, (b) at applied voltage $V=+4500$ V (forward bias: electric field parallel to polarization inside the hexagonal domains), and (c) at applied voltage $V=-4400$ V (reverse bias: electric field antiparallel to polarization inside the hexagonal domains). The domain outlines as seen for $V=0$ are shown in (b) and (c). The small arrows show the apparent motion of defect features from the position at $V=0$.

fields are a result of the interaction of point defect complexes with the domain wall.

IV. DOMAINS IN THE PRESENCE OF AN ELECTRIC FIELD

We now describe the evolution of these domain wall strains under a uniform external field. These experiments were conducted on a congruent *z*-cut crystal of thickness 0.5 mm after the amorphous carbon electrodes were deposited as described above. The measured rocking curve width of the (00.12) Bragg reflection with electrodes in the region of the image was $\Delta\theta_B=110$ μrad as observed previously, although at places on this sample, rocking curves showed structure resolvable into individual Bragg peaks with widths of 27.2 μrad. Figure 2 shows topographs with applied voltages of (a) 0 V, (b) +4500 V, and (c) −4400 V. Figure 2(a) clearly shows several hexagonal ferroelectric domains in addition to numerous dislocations and defects within an extinction depth of the surface of the $LiNbO_3$ crystal. Figure 2(b) shows an apparent growth in domain size as well as a decrease in spacing between the domains. The apparent growth is a consequence of the application of a forward bias (positive voltage: applied electric field **E** parallel to the polarization $\mathbf{P_s}$ inside the hexagonal domains). The domains as observed with no applied field in Fig. 2(a) are shown in outline. Figure 2(c) shows an apparent shrinkage of the domains as well as an increase in the spacing between the domains. The apparent shrinkage is the consequence of the application of a reverse bias state (negative voltage; applied electric field **E** opposite to the polarization $\mathbf{P_s}$ inside the hexagonal domains).

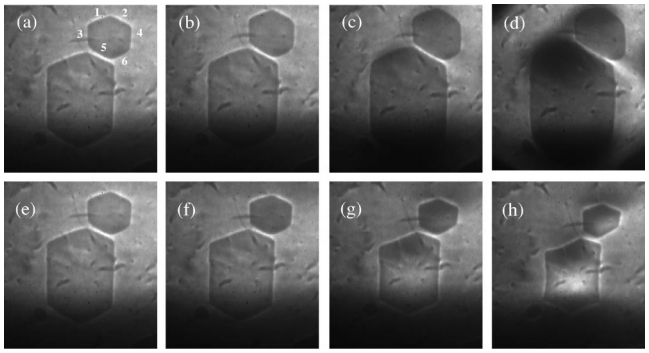

FIG. 3. Details of the (00.12) Bragg topograph for positive applied voltage (forward bias) of (a) 0 V, (b) +1500 V, (c) +3000 V, and (d) +4500 V; for negative applied voltages (reverse bias) of (e) 0 V, (f) −1500 V, (g) −3000 V, and (h) −4400 V.

The coercive field for domain reversal in congruent $LiNbO_3$ single crystals is ~240 kV/cm in the forward bias state and ~150 kV/cm in the reverse bias state. The difference arises from the presence of internal fields as reported before.[19] Since our application of ±90 kV/cm is considerably lower than the coercive fields for $LiNbO_3$, no domain wall motion is expected, consistent with prior *in situ* optical experiments.[13] To check this, we verified using optical microscopy after the experiment that the ferroelectric domain walls had not moved at all by the application of the field. To clarify the effect in the topographs, we tracked the changes in the apparent positions of dislocation features as a result of the application of the external field. These deviations between the initial state of no applied voltage and the final state of high applied voltage are shown as small arrows in Figs. 2(b) and 2(c). Under close inspection we see no major evidence of domain walls crossing dislocations as a result of voltages applied here. Furthermore, in Fig. 2(b) we see apparent expansion of the distance between dislocations in domains with the application of forward bias, and the contraction of the distance between dislocations in the intervening matrix. In Fig. 2(c) we see the opposite effect, the apparent contraction of the distance between dislocations within a domain under the action of a reverse bias, and the expansion of the distance between dislocations in the intervening matrix.

It is significant that dislocation features far away from domain walls show the least apparent motion under the application of the field, independent of whether inside or outside a domain. Figure 3 shows an enlarged view of a domain region under the application of a forward bias of (a) 0 V, (b) +1500 V, (c) +3000 V, and (d) +4500 V. The bias was then returned to (e) 0 V, and we applied reverse biases of (f) −1500 V, (g) −3000 V, and (h) −4400 V. The x-ray images of the hexagonal domains appear to be growing continuously

from Fig. 3(a) to Fig. 3(d), and appear to be shrinking continuously from Figs. 3(e)–3(h).

In summary, we have observed large relative changes in apparent domain size as well as distance between domains as a result of applied electric fields less than the coercive field. The apparent growth or shrinkage of domain walls are never observed to cross dislocations or other defects, and the change in the apparent position of any random feature (such as a dislocation) in the images of Fig. 2 is directly dependent on its proximity to a domain wall.

V. MODELING AND ANALYSIS

The symmetry of $LiNbO_3$ is trigonal $(3m)$. For a z-cut crystal with large surfaces normal to the z-axis, the only nonzero piezoelectric coefficient is d_{333} along the z axis.[15] In the tensor notation, the piezoelectric strain is given by $\varepsilon_{jk} = d_{ijk}E_i$, where E_i is the applied electric field, and d_{ijk} is the relevant piezoelectric tensor coefficient. For a uniform applied field E_3, (where 3 refers to the z axis of $LiNbO_3$), the piezoelectric strain ε_{33} is given by $\varepsilon_{33}=d_{333}E_3$, which therefore depends on the sign of E_3 and d_{333}. The field E_3 is positive when it is parallel to the polarization direction $\mathbf{P_s}$ $(+z$ axis) of a domain region, and E_3 is negative when it is antiparallel to $\mathbf{P_s}$. Since d_{333} is positive for $LiNbO_3$, in the forward bias field (E_3 parallel to $\mathbf{P_s}$ inside the hexagonal domains and antiparallel outside), the matrix shrinks in the z direction (negative ε_{33}) and the regions inside of the hexagonal domains expand along z direction (positive ε_{33}).

Before proceeding further with discussing piezoelectric strains, we note the distinction between piezoelectric and electrostrictive strains. Electrostrictive strain, $\varepsilon_{\mathrm{el}}$ (also called spontaneous strain) in the context of this paper, occurs due to atomic movements that give rise to a spontaneous polarization, $\mathbf{P_s}$ in the crystal and requires no external field. In calculating the strain tensor, we observe that $\varepsilon_{\mathrm{el}} \propto \mathbf{P_s}^2$. The piezoelectric strain, ε_p arises from the interaction between an external electric field, E and the polarization P_s, $\varepsilon_p \propto \mathbf{E}\cdot\mathbf{P_s}$. Far away on either side of a 180° domain wall, $\varepsilon_{\mathrm{el}}$ has the same magnitude and sign; it varies only in the wall region itself, in response to the variation of the polarization magnitude. On the other hand, the piezoelectric strain, under a uniform external field, $+E$, though possessing symmetric magnitude about the wall center, reverses sign across the domain wall. Solving for these strains under elastic compatibility conditions, one finds that the $\varepsilon_{\mathrm{el}}$ (under no external field) is confined in width to the same length scale over which the polarization varies, while ε_p (under a uniform external field E) results in a broad piezoelectric shear strain, ε_{zu} adjacent to domain walls. The lateral width and magnitude of the piezoelectric shear strain ε_{zu} increases proportional to the external electric field and deforms the surface (0001) lattice planes across a domain wall. In the present case, for forward bias field, the hexagonal domain regions in lithium niobate bulge and behave as convex mirrors for x rays in Bragg geometry. This is schematically shown in Fig. 4. Under a reverse bias field they adopt a concave curvature and focus the diffracted x-ray beams. This is also consistent with the observation that the interior of the large hexagonal domain becomes dark under forward bias [in Fig. 3(d)], and bright under reverse bias [Fig. 3(h)].

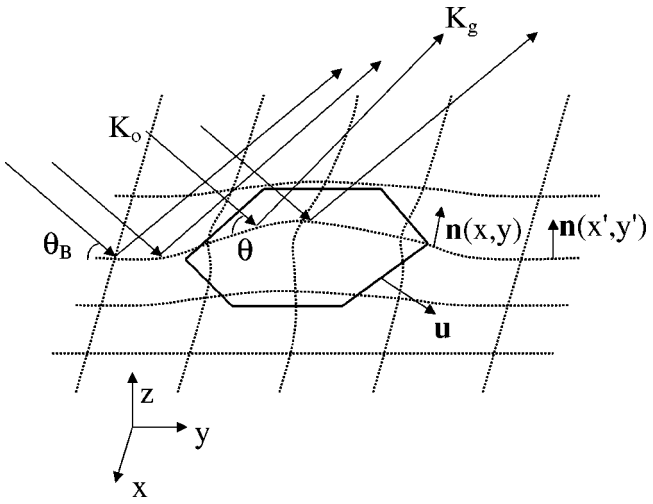

FIG. 4. Surface of a 180° domain showing the surface normal and the effect on kinematical diffraction of an incident x-ray beam.

To understand quantitatively the influence of piezoelectric strain at domain walls on the distortion of x-ray images in Fig. 3, we have performed strain calculations using commercial finite element analysis (FEA) software. As inputs to the calculation, we use reported single crystal values for piezoelectric and elastic stiffness tensor coefficients for $LiNbO_3$.[20] We define a sharp domain wall by inverting the crystallographic z- and the y-axes across a wall. A finite sample has stress-free boundary conditions. After exact calculations of the lattice displacements at the domain walls using FEA software, we calculate the lattice normal vector for (0001) planes at all the walls with an external electric field.

The calculated local surface lattice normal was then used as the input to a ray-tracing program, assuming kinematical diffraction to simulate the actual x-ray image of the distorted sample surface. The ray tracing is similar to a previously reported method[21] for screw dislocation analysis, assuming that the lattice distortions at the crystal surface are primarily contributing to the reflected image. We use a parallel input beam and track the diffracted intensity based on deviation from the Bragg condition. If $\vec{K}_o$ is the incident x-ray wave vector, and $\vec{K}_G$, the diffracted x-ray wavevector, then for slight strains the local reciprocal lattice vector $\vec{G}$ follows the local surface normal. From simple geometrical considerations for small strains,

$$\vec{K}_G = \vec{K}_o - 2(\vec{K}_o \cdot \hat{n})\hat{n}, \tag{1}$$

where $\hat{n}$ is the local unit surface normal vector for (0001) lattice planes. From the surface displacement data obtained from FEA, we calculate the surface normal vector $\hat{n}$ of the distorted surface lattice of a crystal, and trace the reflected x ray wave vector $\vec{K}_G$. At the detector, we simply count the arriving flux of the diffracted beam.

Figure 5 shows (a) the calculated strain and (b) the simulated x-ray topograph under a forward bias field of 90 kV/cm. In this case, the magnitudes of the normal strain ε_{33} are

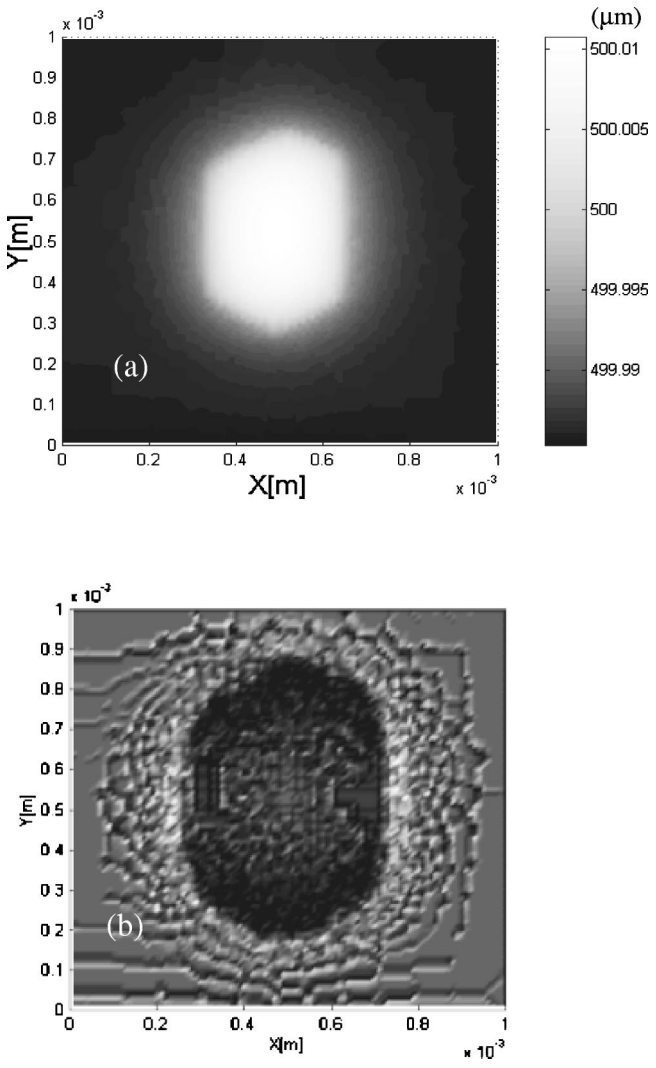

FIG. 5. (a) Calculated surface displacement and (b) calculated (00.12) diffracted ray projection from the domain for $V=+4400$ V (forward bias).

$+5\times10^{-5}$ (domain) and -5×10^{-5} (matrix), and the shear strain ε_{zx} is $\pm2\times10^{-4}$, where the piezoelectric coefficient $d_{333}=0.6\times10^{-11}$ C/N. The width of the shear strain region is about 100 μm, and the step between walls is about 25 nm. The domain wall itself is located in the region of maximum shear strain, and does not actually move. The calculated strain and x-ray images demonstrate respectively, a bulge normal to the crystal surface, and the domain with apparently convex walls as was recorded with increasing field in Figs. 3(b)–3(d). The increased contrast arises primarily from the field induced ε_{zu} piezoelectric strain at the walls. Only a shear strain component can change the shapes of x-ray domain images. As observed, this strain destroys the Bragg condition most effectively at domain wall types 1, 2, 5, and 6 that are at an angle to the incidence plane. It is weak at walls 3 and 4, which are parallel to the incidence plane.

The other contrast mechanism under an external field at all wall types arises from the change in the lattice parameter c with strain ε_{33}. In the forward bias, c increases inside the hexagonal domains, while it decreases in the matrix domain.

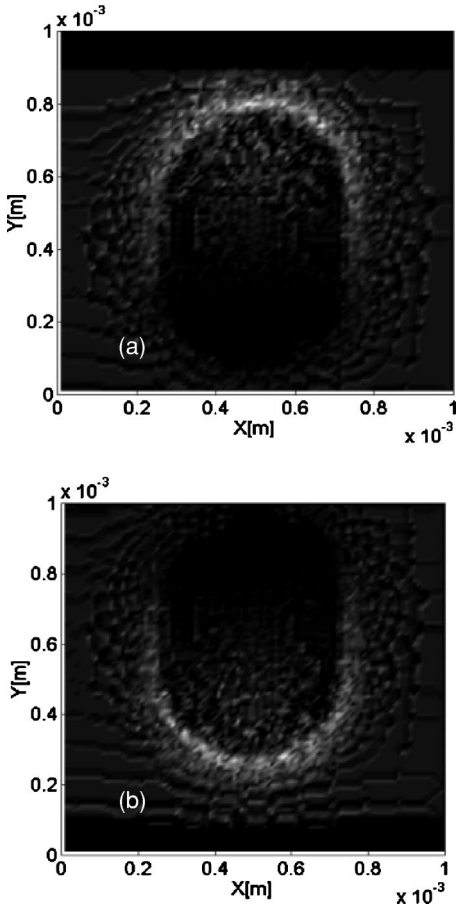

FIG. 6. Calculated ray projection of (00.12) diffraction from the vicinity of the 180° domain in Fig. 5 for (a) $\theta=\theta_B-0.005°$ and (b) $\theta=\theta_B+0.005°$.

With a reverse field bias, the opposite is true. This lattice constant variation only changes contrast rather than changing image shape. A compression or expansion of the lattice parameter is the equivalent of an effective change in the Bragg angle $[\Delta\theta_B=-(\Delta c/c)\tan\theta_B=-\varepsilon_{33}\tan\theta_B]$ which enhances the domain contrast. For the values of ε_{33} calculated above, we would expect the application of $+4500$ V to shift the Bragg angle by $\Delta\theta_B=\pm40$ μrad for a domain and surrounding matrix, respectively. This is significant compared to the observed rocking curve width.

Simulated x-ray topographic images for the rocking curve angles $\theta_B=\pm0.005°$ are shown in Figs. 6(a) and 6(b). The simulated topographs accurately demonstrate the bright and dark contrast of different sets of domain walls arising from domain edge curvature effects similar to what is seen in Figs. 1(a) and 1(c) without any external field. However, we note specifically that the domain wall curvature effects in Fig. 1 are under zero external electric field and are intrinsic to the material (with its point defects). The curvature effects in Fig. 6, on the other hand, are extrinsic in that they arise from the piezoelectric effect due to the application of a uniform external electric field.

The calculated strain and simulated x-ray images under a reverse bias of 90 kV/cm are shown in Figs. 7(a) and 7(b), respectively. In addition to a dimpling of the surface rather

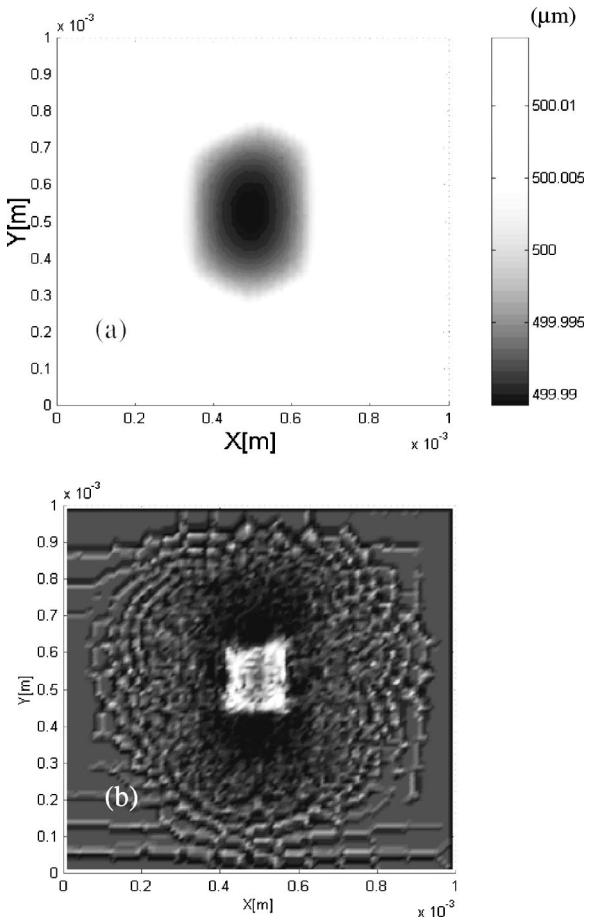

FIG. 7. (a) Calculated surface displacement and (b) calculated (00.12) diffracted ray projection from the domain for $V=-4400$ V (reverse bias).

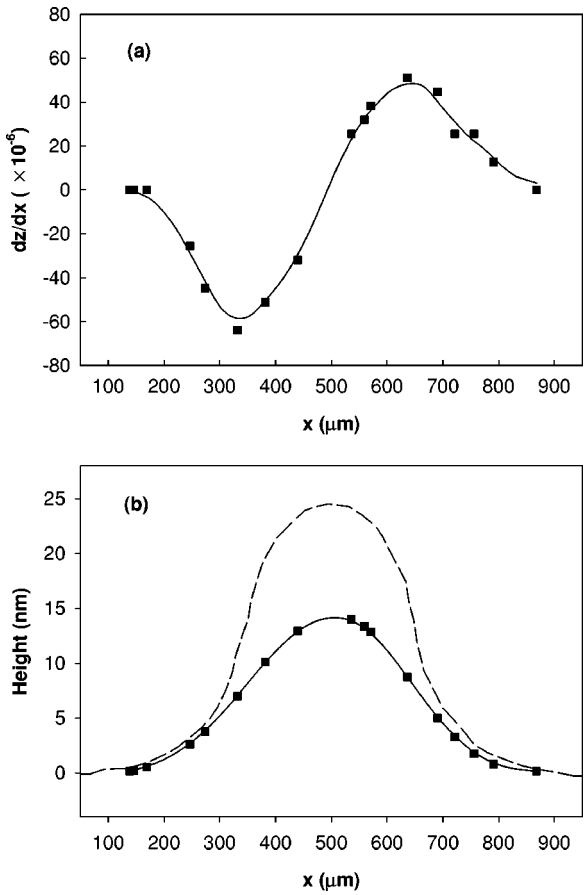

FIG. 8. (a) Surface strain with forward bias measured by a displacement of details between Figs. 3(d) and 3(a) by a line scan across a 180° domain in $LiNbO_3$. The line is a spline fit to the measured points. (b) Positive surface displacement (solid line) derived by integrating curve (a). The dashed line is the predicted effect using bulk coefficients and a finite element calculation at room temperature.

than a bulge, the calculations indicate that domain walls would appear concave as was recorded with increasing reversed field in Figs. 3(f)–3(h).

A careful quantitative analysis of the data, however, reveals that the extent of expansion or contraction in the simulated image exceeds that seen in experiments, suggesting that the actual experimental surface displacements and shear strains at the domain walls may be smaller than the values calculated from the FEA simulation. The surface displacements and strains were obtained from measurements of the experimental images. Starting with Fig. 3(a) that corresponds to zero field-induced strain as the reference, and comparing with the strained images of Figs. 3(d) and 3(h), we measured the displacement at every point on a horizontal line scan across the large hexagonal domain, tracking the movement of dislocations and defects. This is shown in Figs. 8(a) (forward bias) and 9(a) (reverse bias) for image strains extracted from Figs. 3(d) and 3(h), respectively, along with smooth spline fits. The domain walls as determined by this transition appear to be of the order of 100 μm thick.

Applying our ray tracing in reverse from the image plane to the sample surface, we calculated the surface normal vector $\mathbf{n}=-f_x\mathbf{i}-f_y\mathbf{j}+\mathbf{k}$, using Eq. (1), where $f_x=\partial z/\partial x$, $f_y=\partial z/\partial y$, and ($\mathbf{i}$, $\mathbf{j}$, and $\mathbf{k}$) are unit vectors along the crystallographic directions $\mathbf{x}$, $\mathbf{y}$, and $\mathbf{z}$ of the matrix domain. This vector gives the shear strain components, ε_{zu}, and the integration of the components gives the profile of the bulge or depression of the domain under the influence of the applied field. Figure 8(b) (solid line) shows the surface domain expansion deduced by integrating the profile in Fig. 8(a). For comparison, the surface expansion calculated from the FEA program for forward field bias is shown as well (dashed line). Figure 9(b) shows the measured surface displacement (solid line) for the reverse bias obtained by integrating the curve in Fig. 9(a) compared with the value from the FEA calculation (dashed line). Even for a 400-μm-wide domain, the maximum displacements observed experimentally, $+14$ and -11 nm, for the forward and reverse bias fields, are only 0.56 and 0.44, respectively, of the calculated values using bulk piezoelectric and elastic constants. The shear strains, ε_{zu} observed experimentally are also suppressed compared to the bulk predictions. The overall experimental piezoelectric response appears then to be significantly lower in magnitude than the calculated response for a single crystal with a uniform d_{333} coefficient throughout and a 400-μm-wide inverted domain region.

There are several reasons to consider for this discrepancy.

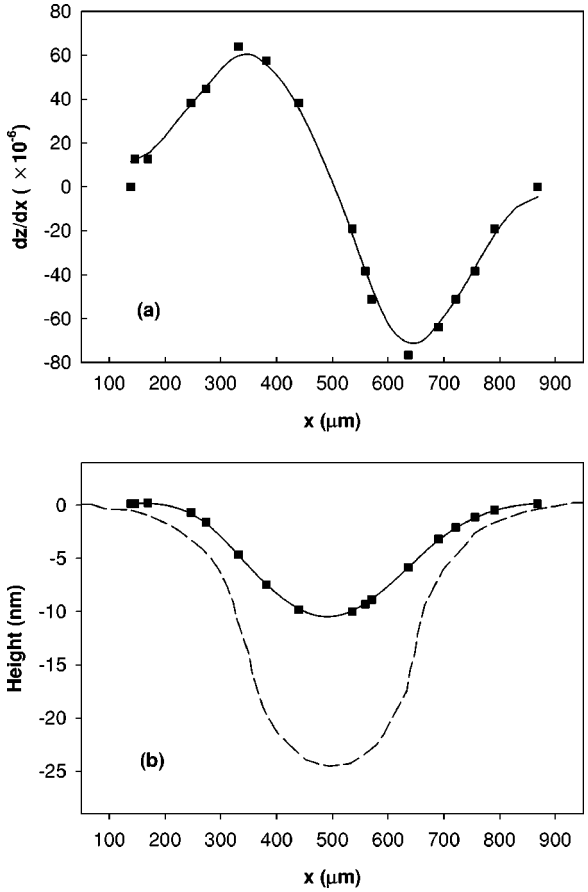

FIG. 9. (a) Surface strain with reverse bias measured by a displacement of details between Figs. 3(h) and 3(a) by a line scan across a 180° domain in $LiNbO_3$. The line is a spline fit to the measured points. (b) Negative surface displacement (solid line) derived by integrating curve (a). The dashed line is the predicted effect using bulk coefficients and a finite element calculation at room temperature.

One possibility is that localized charge states near the surface of the insulating crystal screen the bulk applied field in the region between the electrodes by more than a factor of 2. A second possibility is that absorbed x rays from the intense x-ray beam during application of the electric field could also locally screen the electric field by creating electron-hole pairs in the material. Though we did observe some photoconductive current with x rays,[22] we were able to rule out a large effect due to this type of screening by measurements with similar graphite electrodes on thinner crystals. In those instances, the measured coercive field for permanent domain reversal under x-ray illumination was close to the actual reported value with water-based electrodes without x rays. A third possibility is that the size of the domain may play a role in the mechanical clamping of the displacement, thus suppressing it. This mechanical compatibility condition is accounted for by FEA, unless the input material parameters are different from the bulk.

It is worth considering the possibility that perhaps the piezoelectric coefficients d_{333} are lower (by about 2), and/or the stiffness coefficients, C_{3333} are higher, in the vicinity of a domain wall. The presence of local strain and wall structure even in the absence of external field (Fig. 1) arising from point defects in these crystals suggests that the variation of defect fields across a wall may play some role in the observed suppression of lattice displacement near the walls. Finally, there is also the possibility of field-induced broadening of the polarization gradient at a domain wall, as has been recently proposed.[23] Since the piezoelectric coefficient d_{333} is linearly proportional to the spontaneous polarization, P_s, a broadened polarization gradient across a domain wall that goes through zero at the center of the wall can locally induce a gradient of d_{333} coefficient across the wall as well, thus suppressing the overall piezoelectric response in that region.

Pernot-Rejmánková, Laprus, and Baruchel have previously described an overall curvature of congruent $LiNbO_3$ resulting in x-ray focusing which did not include the effect of visible stable domains.[15] That effect was observed in fields applied across *x*- and *y*-cut crystals but not *z*-cut crystals and their explanation requires the assumption of an inhomogeneous crystal. The behavior observed here in a *z*-cut crystal was consistent with the assumption of a single piezoelectric coefficient.

VI. CONCLUSIONS

The important conclusions of this work regarding domain walls in congruent $LiNbO_3$ at room temperature are as follows. In the absence of an applied external field, there exists a shear strain of the order of $\varepsilon_{zx} \approx \pm 6.0 \times 10^{-5}$ at these domain walls. This results in a lattice step of $\sim$0.6 nm over a 10-μm lateral distance between the two domains separated by the domain wall. Under an external bias, piezoelectric strains result in normal strains $+\varepsilon_{33}$ and $-\varepsilon_{33}$ across a wall, resulting in an increased shear strain ε_{zx}, whose lateral extent can exceed 100 μm. In neither circumstance can the observed domain wall strains be described as abrupt or highly localized. The effect of applied fields results in a net bulging or dimpling of the 180° domain at both crystal surfaces, depending on the polarity of the field with respect to the polarization direction in the domain. There is evidence that the observed strains are, in practice, substantially lower than that predicted using mechanical compatibility conditions and bulk values of single domain piezoelectric and elastic stiffness tensor coefficients. It is possible to account for this experimentally by electrostatic screening of the applied field due to surface states. The reduced response is also consistent with local electromechanical properties in the vicinity of a 180° domain wall that may be different from the bulk values.

Our work suggests that ferroelectric domains can behave as ''x-ray mirrors'' for the focusing and defocusing of x-rays at the Bragg condition as a result of electric fields applied to the ferroelectric crystals.

ACKNOWLEDGMENTS

The authors would like to acknowledge helpful discussions with Dr. B. Steiner. Portions of this work were con-

ducted at the Advanced Photon Source at Argonne National Laboratory. We thank Dr. R. Cook for aid in electrode deposition and Dr. A. Mashayekhi and the SRI-CAT for assistance on the 1-ID and 4-ID Beamlines. Use of the Advanced Photon Source was supported by the U.S. Department of Energy, Office of Science, Office of Basic Energy Sciences, under Contract No. W-31-109-Eng-38. The Penn State authors would like to acknowledge support from the National Science Foundation Grant Nos. DMR-9984691 and DMR-0103354.

[1] R. G. Batchko, V. Y. Shur, M. M. Fejer, and R. L. Byer, Appl. Phys. Lett. **75**, 1673 (1999).
[2] K. T. Gahagan, V. Gopalan, J. M. Robinson, Q. X. Jia, T. E. Mitchell, M. J. Kawas, T. E. Schlesinger, and D. D. Stancil, Appl. Opt. **38**, 1186 (1999).
[3] V. A. Zhirnov, Zh. Eksp. Teor. Fiz. **35**, 1175 (1958) [Sov. Phys. JETP **35**, 822 (1959)].
[4] A. Gordon, Physica B **122**, 321 (1983).
[5] W. Cao and G. R. Barsch, Phys. Rev. B **41**, 4334 (1990).
[6] J. Padilla, W. Zhong, and D. Vanderbilt, Phys. Rev. B **53**, 5969 (1996).
[7] X. R. Huang, X. B. Hu, S. S. Jiang, and D. Feng, Phys. Rev. B **55**, 5534 (1997).
[8] R. C. Miller and G. Weinreich, Phys. Rev. **117**, 1460 (1960).
[9] M. Foeth, P. Stadelmann, and P.-A. Buffat, Ultramicroscopy **75**, 203 (1999).
[10] J. Wittborn, C. Canalias, K. V. Rao, R. Clemens, H. Karlsson, and F. Laurell, Appl. Phys. Lett. **80**, 1622 (2002).
[11] M. Drakopoulos, Z. W. Hu, S. Kuznetsov, A. Snigerev, I. Snigereva, and P. A. Thomas, J. Phys. D **32**, A160 (1999).
[12] P. Lerner, C. Legras, and J. P. Dumas, J. Cryst. Growth **3/4**, 231 (1968).
[13] T. J. Yang and U. Mohideen, Phys. Lett. A **250**, 205 (1998).
[14] S. Kim, V. Gopalan, and B. Steiner, Appl. Phys. Lett. **77**, 2051 (2000).
[15] P. Pernot-Rejmánková, W. Laprus, and J. Baruchel, Eur. Phys. J.: Appl. Phys. **8**, 225 (1999).
[16] P. Rejmánková, J. Baruchel, P. Moretti, M. Arbore, M. Fejer, and G. Foulon, J. Appl. Crystallogr. **31**, 106 (1998).
[17] V. Gopalan and T. E. Mitchell, J. Appl. Phys. **85**, 2304 (1999).
[18] S. Kim, V. Gopalan, K. Kitamura, and Y. Furukawa, J. Appl. Phys. **90**, 2949 (2001).
[19] V. Gopalan, T. E. Mitchell, Y. Furukawa, and K. Kitamura, Appl. Phys. Lett. **72**, 1981 (1998).
[20] *Ferroelectrics and Related Substances*, edited by K. H. Helwege, Landolt-Bornstein, New Series, Group III, Vol. XVI (Springer-Verlag, Berlin, 1961).
[21] X. R. Huang, M. Dudley, W. M. Vetter, W. Huang, W. Si, and C. H. Carter, Jr., J. Appl. Crystallogr. **32**, 516 (1999).
[22] T. Jach, S. Kim, S. Durbin, V. Gopalan, and D. Bright, in *Fundamental Physics of Ferroelectrics 2002*, edited by R. E. Cohen (AIP, Melville, NY, 2002), Vol. 626, p. 269.
[23] S. Kim, V. Gopalan, and A. Gruverman, Appl. Phys. Lett. **80**, 2740 (2002).